IEEE Access
Multidisciplinary | Rapid Review | Open Access Journal

Received 31 March 2023, accepted 13 April 2023, date of publication 17 April 2023, date of current version 24 April 2023.

Digital Object Identifier 10.1109/ACCESS.2023.3267814

RESEARCH ARTICLE

Depth Recovery With Large-Area Data Loss Guided by Polarization Cues for Time-of-Flight Imaging

YUWEI ZHAO[1], XIA WANG[1], YUJIE FANG[2], AND CHAO XU[1]

[1]Key Laboratory of Photoelectronic Imaging Technology and System, Ministry of Education of China, School of Optics and Photons, Beijing Institute of Technology, Beijing 100081, China
[2]Beijing Institute of Technology, Zhuhai 519000, China

Corresponding author: Xia Wang (angelniuniu@bit.edu.cn)

This work was supported in part by the National Natural Science Foundation of China under Grant 62031018.

ABSTRACT Time-of-Flight imaging is one of the quintessential techniques in three-dimensional reconstruction. However, depth missing is a common problem in Time-of-Flight imaging, which can be classified into structure-based depth loss and large-area one according to various reasons. Large-area depth loss generally occurs due to close-range overexposure resulting in limited dynamic range in depth sensing. Compared to structure-based depth loss, the recovery of large-area depth missing is more challenging and has been rarely studied. In this paper, a large-area depth recovery framework guided by polarization cues is proposed stemmed from a solid physical basic concerning depth and polarization, to realize high dynamic range in applications. Inspired by RGB-D system and shape-from-polarization technique, a dual camera system is utilized including infrared Time-of-Flight camera and visible polarized camera. A physical model between depth map and polarization cues, specifically depth-gradient and degree-of-polarization, is investigated and established. Based on the physical basics, a corresponding polarization-guided depth recovery algorithm with statistical analysis and image processing approach is introduced. Experimental results towards different targets demonstrate the effectiveness of the proposed method qualitatively and quantitatively, accompanied with outcome analysis and detailed discussions about strengths and future works, which indicates a great potential for the applications of high-quality three-dimensional reconstruction and depth sensing.

INDEX TERMS Depth recovery, time-of-flight imaging, polarization cues.

I. INTRODUCTION

Three-dimensional (3D) reconstruction is of considerable significance in various domains, e.g. heritage restoration in historical preservation [1], indoor survey in architectural design [2], environmental construction for autonomous driving [3], etc., because of its superiority in non-contact, high efficiency and cost-effectiveness. Plenty of techniques with different methods are applied in 3D reconstruction which have made great contributions in civil and scientific fields [4]. Time-of-Flight (TOF) imaging is one of the trending active approaches for 3D reconstruction to obtain depth maps of the surveyed scenes due to its advantages of being highly compact, low power consumption, low cost, and real-time. TOF is a typical ranging method demodulating depth information from the received signal. The development of TOF sensor makes TOF imaging realizable at a video frame rate without scanning mechanism [5].

However, TOF imaging suffers from technical shortcomings in practice limited by its working mechanism. Depth missing is one of the major inherent problems resulting in considerable holes in depth maps as shown in Fig.1 intuitively, leading to significant information loss and incomplete 3D reconstruction for applications. Depth missing in

The associate editor coordinating the review of this manuscript and approving it for publication was Mehul S. Raval.

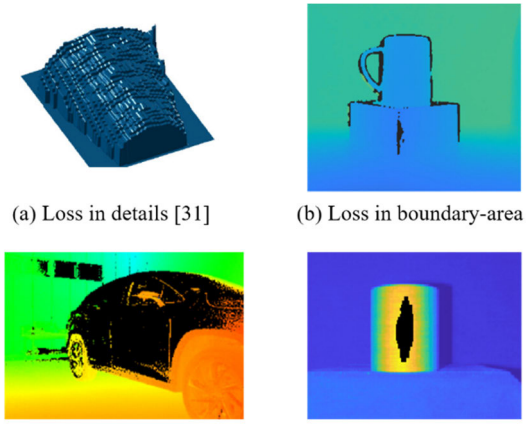

(a) Loss in details [31] (b) Loss in boundary-area

(c) Loss at specular surface [30] (d) Loss due to overexposure

FIGURE 1. Typical depth loss conditions in TOF imaging due to various reasons.

TOF imaging is generally induced by four types of reasons, that is, the low resolution of the up-to-date TOF sensors, discontinuity in edge-area, insufficient power reflection for specular surface or surface with relatively low reflectivity at infrared frequency, and overexposure for short-range measurements, as shown in Fig.1 respectively. More specifically, overexposure for close-range measurements means limited dynamic range in depth sensing, that is enough power for remote sensing will lead to overexposure in close-range detection. Among all those reasons, holes in the first two cases are slight and highly correlated with the nearby structures, namely structure-based, which means it's comparatively easy to recover according to the known data of the neighborhood. While, for the last two cases, depth loss is commonly in large-area and shares limited similarity with the known neighborhood, which is more challenging to be recovered accurately. Many studies pay attention to depth recovery under low-resolution and discontinuous conditions rather than the inpainting of large-area depth missing.

Meanwhile, the character of polarization is of great importance in optical imaging and measurements. As the production of polarized sensors, polarization cues can be simply acquired after calculations based on intensity images with four distinct polarization orientations, from only one shot, which makes polarized imaging convenient and prevailing. As a passive approach, polarized imaging in visible and infrared spectrum plays a critical role in specific circumstances, like underwater imaging [6], image dehaze [7], etc. In 3D imaging fields, polarization cues are also used in different types of depth sensing techniques such as stereo vision [8], [9], structured light [10], [11] and TOF imaging [12], [13], achieving better performance in challenging conditions. Besides, Shape-from-Polarization (SfP) is a classical method for shape acquisition based on polarization cues [14]. The principle of SfP presents a solid physical basic between polarization and shape information, which is the motivation of large-area depth recovery via polarization-guided approach.

This paper proposes a polarization-guided depth recovery algorithm for active TOF imaging accompanied with passive polarized imaging (Pol-D system) to deal with large-area data missing for high dynamic range depth sensing and high-quality 3D reconstruction. Specifically, the proposed algorithm stems from two facts. Firstly, data missing only occurs in TOF sensors due to its active working principle, rather than in the passive polarized imaging side, meaning that comprehensive capture of the reconstructed scene is available from the polarized image which can instruct the recovery of the incomplete depth map. Secondly, the Degree-of-Polarization (*DOP*) property resolved from the polarized images has an intrinsic physical relationship with the shape, namely depth map, of the surveyed scene, which provides a solid basis for polarization-guided depth recovery. Experiments verify that polarization-guided approach has an outstanding performance in large-area depth recovery in practice. The contributions of the proposed method are summarized in following aspects:

- A physical model between polarization cue and depth map is established, in which polarization cue refers to Degree-of-Polarization (*DOP*). According to Fresnel's equation, *DOP* is the function of the partial derivative of the depth map with modifications and approximations, which is derived in Section III.
- An image processing algorithm for polarization-guided depth recovery is proposed. Based on the aforementioned physical model, an algorithm including statistical analysis, image filtering and polarization-depth look-up-table construction is illustrated in Section IV.
- A polarization-guided large-area depth recovery framework for time-of-flight imaging is provided. The validity and generality are verified through experiments, and the performance is compared with relative depth recovery approaches in Section V.

II. RELATED WORK

With the rapid growth in 3D imaging techniques and 3D reconstruction applications, depth recovery methods for high-quality depth sensing are considerably investigated in previous research [15]. The existing methods can be classified into two categories according to whether the depth map is self-repaired or repaired with guidance from additional sources. Self-repaired approaches recover the missing data from the known area of the incomplete depth map through morphological filtering [16], improved low-rank matrix completion with low gradient regulation [17], or deep learning method [18]. In addition, since TOF imaging can obtain depth map and infrared intensity images simultaneously, Yong Sun Kim realized depth recovery by minimizing an energy function utilizing both depth and infrared data [19]. Due to the limited information contained in the depth map, a majority of attempts restore the depth hole with the support of high-quality color images captured by another optical sensor, especially as the RGB-D camera like Kinect v2 came to sell. The high-frequency components in the texture [20]

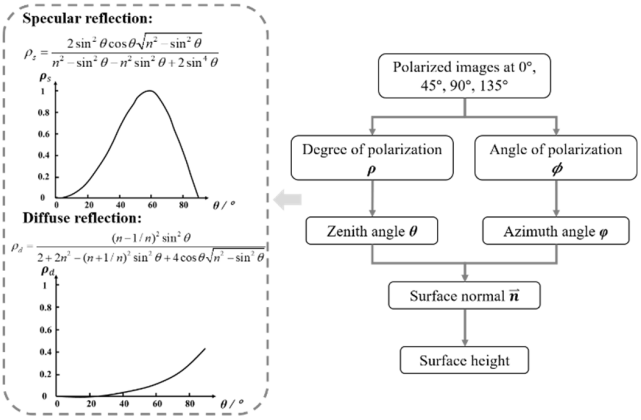

FIGURE 2. General steps of shape-from-polarization in 3D reconstruction.

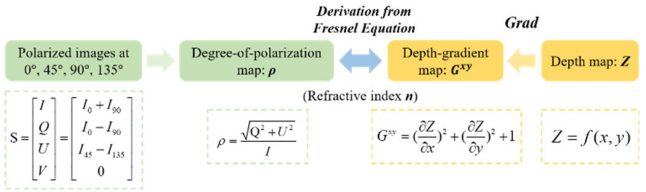

FIGURE 3. A brief summary of the physical relation between depth and polarization cues.

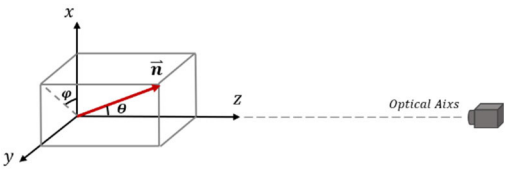

FIGURE 4. Geometric model of target surface in polarized imaging under camera coordinate.

or boundary area of the color image [21], [22], where depth data usually lose, could guide the recovery of depth map and achieving super-resolution or denoise in 3D reconstruction furthermore. A texture-dependent large-area depth recovery for RGB-D camera has been studied in [23]. Liu [24] and Zhang [25] implemented Fast Marching Method (FFM) in RGB-guided depth recovery. Fei proposed a non-local guided-filter [26]. Others developed mathematical models between depth cues and color images, for example, RGB-guided adaptive autoregressive model [27], image guided total generalized variation model [28] and energy minimization model [29]. Deep learning method is also available in RGB-D framework [30]. However, most of the previous RGB-D methods focus on slight depth missing occurred in boundary area rather than large-area as shown in Fig.1 (c)-(d).

Besides, Yoshida has paid attention to large-area depth missing in TOF imaging caused by specular reflection, combining Shape-from-Polarization (SfP) technique [31], since SfP could reconstruct surfaces through polarized images independently. Kadambi also improved the quality of TOF imaging with the help of SfP [32], [33]. In those two methods, an RGB-D framework is replaced by Pol-D system which has a more comprehensive shape understanding of the surveyed scenes with the help of polarization cues.

Nevertheless, SfP suffers from difficulties in practice in the above polarization combined methods. The general process of SfP is summarized in Fig.2 [34]. The challenges in SfP can be divided into several parts. Firstly, ambiguity happens in the calculation of the zenith angle for specular objects. Researchers dealt with this problem through measurements in multiple viewpoints [35], multi-spectra polarized imaging [36], mathematical modeling and optimization [6], etc. Besides that, ambiguity in azimuth angle occurs in both specular and diffuse objects. Methods concerning multi-source illumination [37], multi-viewpoint capture [38], combination with additional 3D imaging approaches [39] and so on. Another challenge launches in the separation of specular and diffuse components, since specular and diffusive reflection have distinct models as shown in Fig.2, it is necessary to identify and separate those elements [40]. Even though the difficulties can be overcome through various approaches, it is still not an optimal choice for polarization-guided depth recovery framework.

III. PHYSICAL BASICS BETWEEN DEPTH DATA AND POLARIZATION CUES

To overcome the sophistication of combining polarized imaging with TOF imaging via SfP, we proposed a *DOP*-guided depth recovery framework based on Pol-D system, skipping the complicated procedures of SfP. The relation between depth and polarization cue is presented in Fig.3, in which the polarized images are collected from a polarized camera in visible spectrum and the depth map is obtained from a TOF camera, shooting the same scene.

The polarization state of the reflected light after interactions with the surveyed target can be described by Stokes vectors, written as (1), and the degree-of-polarization can be calculated through (2)

$$\mathrm{S} = \begin{bmatrix} I \\ Q \\ U \\ V \end{bmatrix} = \begin{bmatrix} I_0 + I_{90} \\ I_0 - I_{90} \\ I_{45} - I_{135} \\ 0 \end{bmatrix}, \tag{1}$$

$$\rho = \frac{\sqrt{\mathrm{Q}^2 + U^2}}{I}. \tag{2}$$

in which, $I_0, I_{45}, I_{90}, I_{135}$ are the intensity of the polarized images under polarization orientations at 0°, 45°, 90°, 135°.

According to Fresnel Equations, the degree of polarization for specular and diffuse reflections are the function of zenith angle θ respectively, in terms of refractive index n [6]:

$$\rho_s = \frac{2\sin^2\theta\cos\theta\sqrt{n^2 - \sin^2\theta}}{n^2 - \sin^2\theta - n^2\sin^2\theta + 2\sin^4\theta}, \tag{3}$$

$$\rho_d = \frac{(n - 1/n)^2\sin^2\theta}{2 + 2n^2 - (n + 1/n)^2\sin^2\theta + 4\cos\theta\sqrt{n^2 - \sin^2\theta}}, \tag{4}$$

in which, ρ_s is the *DOP* of specular surface and ρ_d stands for diffusive reflection, n is the refractive index of the target.

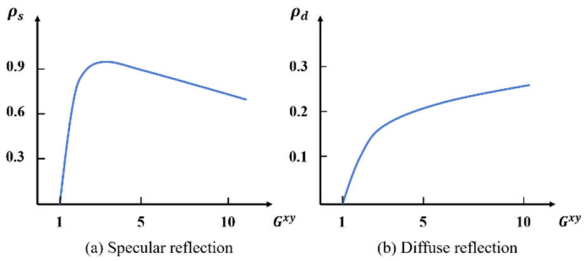

FIGURE 5. Functional relationship between degree-of-polarization and depth-gradient for specular and diffuse reflections.

Zenith angle θ is the incidence or emittance angle in reflection, approximately it can be considered as the angle between the surface normal $\vec{n}$ and the optical axis of the camera, as shown in Fig.4.

From the view of TOF side, the depth map Z can be seen as a two-dimensional function in pixel coordinates (or x-y coordinate in Fig.4) of the imaging plane

$$Z = f(x, y). \tag{5}$$

Mathematically, the surface normal of the surveyed scene is expressed as

$$\vec{n} = (-f_x'(x, y), -f_y'(x, y), -1) = (-\frac{\partial Z}{\partial x}, -\frac{\partial Z}{\partial y}, 1). \tag{6}$$

As the zenith angle is in between z-axis and $\vec{n}$, it can be expressed in regard to depth Z:

$$\cos\theta = \frac{1}{\sqrt{(-f_x'(x, y))^2 + (-f_y'(x, y))^2 + (1)^2}}. \tag{7}$$

A ***Grad*** operator and a corresponding parameter G^{xy} representing the *depth-gradient* are proposed in this paper, to simplify the physical relation among polarization cue and depth data

$$\begin{aligned} G^{xy} &= Grad(Z) = (f_x'(x, y))^2 + (f_y'(x, y))^2 + (-1)^2 \\ &= (\frac{\partial Z}{\partial x})^2 + (\frac{\partial Z}{\partial y})^2 + 1. \end{aligned} \tag{8}$$

Combining (8) and (7), zenith angel θ can be expressed in both cosine and sine form,

$$\cos\theta = \sqrt{\frac{1}{G^{xy}}}, \sin\theta = \sqrt{\frac{G^{xy} - 1}{G^{xy}}}. \tag{9}$$

The relations between degree-of-polarization (*DOP*) and *depth-gradient* are formed for specular and diffusive surface separately after substituting (9) into (4) and (5)

$$\rho_s = \frac{2(G^{xy} - 1)\sqrt{n^2 G^{xy} - G^{xy} + 1}}{G^{xy2} + (n^2 - 3)G^{xy} + 2}, \tag{10}$$

$$\rho_d = \frac{(n - 1/n)^2 (G^{xy} - 1)}{(n^2 - 1/n^2)G^{xy} - (n + 1/n)^2 + 4\sqrt{n^2 G^{xy} - G^{xy} + 1}}. \tag{11}$$

As shown in (10)-(11), refractive index, n, is an additional parameter in the relation of polarization and depth cues, which is determined by the material of the target. The $\rho - G^{xy}$ relations are depicted in curves in Fig.5.

In the polarization-guided depth recovery scenario where depth data is partially missing (Fig.1(c) & (d)) and polarized information is flawless, refractive index, n, can be estimated from region with known depth and polarization cues. For regions with depth holes, the missing depth can be recovered via measured *DOP* and estimated n. However, strict mathematical estimation and calculation of n and G^{xy} according to (10)-(11) are computational and sophisticated since both G^{xy} and n are unavailable to be expressed by elementary functions without simplifications or approximations. On the other hand, the accuracy of the refractive index estimation is affected by the noisy and unideal polarized images and *DOP* calculation. And, furtherly, the calculation of *depth-gradient* for the depth missing area is influenced by the inaccurate estimated refractive index, which means the depth recovery method directly based on $\rho - G^{xy}$ relation is susceptible to noise in practice. In addition, in specular cases, ρ and G^{xy} do not have a one-on-one relation, which leads to undesired ambiguities in calculation as shown in Fig.5.

In conclusion, with complete polarized information, depth loss can be repaired by solving (10) and (11) in a mathematical way, yet with difficulties. An algorithm with statistics and imaging process approaches is introduced in the next section, skipping the estimation of refractive index and acquiring depth data under polarization guidance accurately and cost-efficiently.

IV. POLARIZATION-GUIDED DEPTH RECOVERY ALGORITHM

The aforementioned physical model between polarization cue, ρ, and depth information, G^{xy}, indicates a solid basis for polarization-guided depth recovery algorithm. The proposed algorithm aims at recovering large-area depth missing caused by overexposure and specular or low-power reflectance. As a prerequisite of the following algorithm, the surveyed target should be partially depth missing instead of entire data loss since the depth recovery is implemented with the guidance of data from depth known area, whereas this requirement is reasonable and common in practice. Moreover, the performance would be better and more accurate if the target is homogenous with stable refractive index and the surface is smooth without any discontinuities.

A. FRAMEWORK OVERVIEW FOR POLARIZATION-GUIDED DEPTH RECOVERY ALGORITHM

Fig.6 demonstrates the framework of the proposed polarization-guided depth recovery algorithm. Depth map with data loss and a group of flawless polarized images including polarization orientation at 0°, 45°, 90°, 135° are the inputs, captured individually by TOF camera and polarized camera in parallel. In the pre-process stage, denoise and stereo calibration of polarized image and depth map are implemented. The real-world distance between adjacent pixels in horizontal and vertical directions, Δx, Δy, at different ranges is calibrated as well. Afterwards, *DOP* and *depth-gradient* are calculated pixel-wise according to

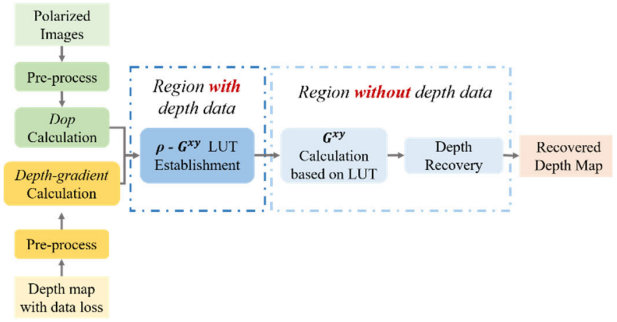

FIGURE 6. Framework overview for polarization-guided depth recovery algorithm.

(1)-(2) and (8). Specifically, partial-gradient operation in (8) is replaced by (12) in practice with the pre-calibrated real-world distance between adjacent pixels,

$$G^{xy} = Grad(Z) \approx (\frac{\Delta Z}{\Delta x})^2 + (\frac{\Delta Z}{\Delta y})^2 + 1. \tag{12}$$

According to the physical basics in Section III, in the region with depth data, a look-up table (LUT) concerning relations between *DOP* and *depth-gradient* is established, to guide the recovery of the data missing area. With constructed LUT, *depth-gradient* of the depth missing region is attainable and depth information is correspondingly recovered.

B. $\rho - G^{xy}$ LUT ESTABLISHMENT

Utilizing the calculated *DOP* and *depth-gradient* map, a LUT could be generated from the region with depth data. A pixel-by-pixel moving window with $N_1 \times N_1$ size is formed as shown in Fig.7(a) and the selection of parameter N_1 is discussed in Section VI. Since ρ and G^{xy} are continuously distributed inside each $N_1 \times N_1$ neighborhood, linear least square (LSM) method is undertaken to solve the statistical relation between ρ and G^{xy} based on $N_1 \times N_1$ groups of polarization and depth data, as illustrated in (13) and Fig.7(b):

$$G^{xy}(\rho)_i = a_{pn} \cdot \rho_i + b_{pn}, \tag{13}$$

in which, a_{pn} and b_{pn} stand for the statistic coefficients in $\rho - G^{xy}$ relation inside n^{th} $N_1 \times N_1$ patch. Coefficients a_{pn} and b_{pn} vary in different patches even with identical ρ_i, therefore, a_{pn} and b_{pn} at certain ρ_i are averaged out among all the patches and collected into a LUT (Fig.(8)). The precision of the LUT is set to be 0.0001, which is the interval between ρ_i and ρ_{i+1}. The range of ρ_i is determined by the global shape of the interested target.

Due to the slight difference in $\rho - G^{xy}$ relation, the size of LUT depends on the shape and material of the target as shown in Fig.8. If specular component contains in the reflectance, minus coefficient a_{pn} may exist according to Fig.5(a) in the LSM step which leads to a $5 \times m$ LUT instead of $3 \times m$ LUT with only positive a_{pn}. In Fig.8(b), the second and third row store the coefficient with positive a_{pn}, while the last two rows save groups of coefficients with negative a_{pn}.

Noted that replacing the estimation of refractive index n mentioned in Section III with $\rho - G^{xy}$ LUT can significantly reduce the complexity of computation and doesn't need the pre-knowledge of reflection type. Most notably, mixture of specular and diffuse reflection is common in practice, while separation and respective treatment for specular and diffusive components are unnecessary in LUT construction, compared with the estimation of refractive index which is strictly based on two independent equations ((10)-(11)). The established LUT could involve both specular and diffusive components in a mixed form, avoiding a complexed mathematical expression when specular and diffuse reflection occur simultaneously.

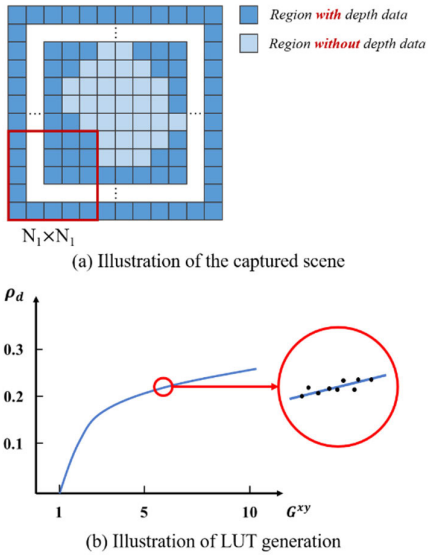

FIGURE 7. Illustrations of the $\rho - G^{xy}$ LUT generation algorithm.

LUT for diffuse target

ρ	$\rho_{i=1}$	$\rho_{i=2}$	.....	ρ_i	.....	$\rho_{i=m}$
a_p	$a_{p_{i=1}}$	$a_{p_{i=2}}$	.....	a_{p_i}	.....	$a_{p_{i=m}}$
b_p	$b_{p_{i=1}}$	$b_{p_{i=2}}$	.....	b_{p_i}	.....	$b_{p_{i=m}}$

(a) Diffuse reflection

LUT for specular target

ρ	$\rho_{i=1}$	$\rho_{i=2}$	.....	ρ_i	.....	$\rho_{i=m}$
a_{p+}	$a_{p_{+i=1}}$	$a_{p_{+i=2}}$	.....	a_{p+i}	.....	$a_{p_{+i=m}}$
b_{p+}	$b_{p_{+i=1}}$	$b_{p_{+i=2}}$	.....	b_{p+i}	.....	$b_{p_{+i=m}}$
a_{p-}	–	–	.....	a_{p-i}	.....	$a_{p_{-i=m}}$
b_{p-}	–	–	.....	b_{p-i}	.....	$b_{p_{-i=m}}$

(b) Specular reflection

FIGURE 8. LUT structures for diffuse and specular reflections.

C. DEPTH-GRADIENT CALCULATION BASED ON $\rho - G^{xy}$ LUT

In the region without depth data, *depth-gradient* is able to be figured out through the established $\rho - G^{xy}$ LUT. For each missing pixel, G^{xy} is computed in a $N_2 \times N_2$ neighborhood:

$$G^{xy}(\rho)_k = a_{pi}(\frac{1}{N_2^2}\sum_{q=1}^{N_2^2} G_\sigma(\|k-q\|) \cdot \rho_q) + b_{pi}, q \in \Omega_{k,N_2}, \tag{14}$$

in which,

$$G_\sigma(x) = \frac{1}{2\pi\sigma^2}\exp(-\frac{x^2}{2\sigma^2}). \tag{15}$$

In (14), k represents the position of the calculated pixel, q is the neighbor pixel within $N_2 \times N_2$ neighborhood Ω_{k,N_2}, σ is the standard deviation of gaussian distribution. The known ρ of the fixed pixel is averaged out in a $N_2 \times N_2$ neighborhood before looking up the LUT, to mitigate the influence of random noise in *DOP* map for reliable noise resistant ability.

Moreover, the $5 \times m$ LUT contains both positive and negative coefficient for a specific ρ_i, the selection of parameter a_{pn} and b_{pn} is instructed by its neighborhood. If the neighboring ρ and G^{xy} values of each point form a positive relationship, then the positive coefficient is chosen and vice versa.

D. DEPTH RECOVERY FROM G^{xy}

For the missing points, with calculated *depth-gradient* from the above procedures, depth data is going to be recovered. Specifically, depth calculation is conducted in a 3×3 neighborhood pixel by pixel in a certain direction as shown in Fig.9(a), ensuring that depth data for at least two pixels in its 4-neighbor are given like ones in Fig.9(b).

In the 3×3 neighborhood, depth difference between the adjacent pixels is first calculated through (16)

$$\Delta Z = \sqrt{\frac{G^{xy}-1}{2}} \cdot \frac{\Delta x + \Delta y}{2}. \tag{16}$$

Then, absolute depth d is available:

$$d = \sum_{j=1}^{N} d_j - \Delta Z, N = 2, 3, 4 \tag{17}$$

in which, $d_j$is the absolute depth in its 4-neighbor which is known or already calculated and there are three conditions for N as demonstrated in Fig.9(b).

V. EXPERIMENTS

The experiments are conducted with a dual-vision imaging system equipped with a polarized color camera from Lucid in visible spectrum and a TOF camera working at 850nm, capturing the same target in parallel as shown in Fig.10. The resolution of the imaging system is set to 360×480.

Several targets with various shape and reflective properties are utilized to verify the effectiveness of the proposed method which are chosen from common stuffs including pottery cup, grapefruit, porcelain vase, paper cup and gift box from (a) to (e). All the selected targets are mixture of specular and diffuse components, in which grapefruit and porcelain vase are specular dominant, while pottery cup, paper cup and gift box are diffuse dominant, in order to verify the generality and superiority of the proposed method, compared with SfP-based approach in [31]. The distance between target and imaging system is roughly 45 cm to 55 cm in depth reconstruction which results in large-area depth missing due to overexposure in close-range. The shape and size of the data

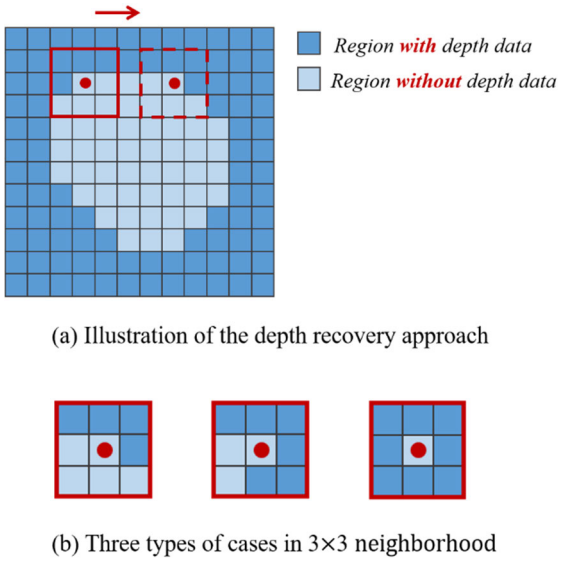

(a) Illustration of the depth recovery approach

(b) Three types of cases in 3×3 neighborhood

FIGURE 9. Illustrations for depth recovery method and different conditions.

FIGURE 10. Pol-D setup for the proposed framework.

loss area are set differently to explore the characteristic and ability of the proposed method.

Fig.11 shows the experimental results before and after depth recovery, including the target shape in RGB format, depth map of original measurements, depth map after recovery using the proposed method and depth in ground-truth. Error map demonstrated the effectiveness of the proposed method within data missing area intuitively. Besides qualitative illustration in depth map, mean absolute error (MAE) between ground-truth and recovered depth inside missing region is used to analyze and validate the capability of the algorithm. An index concerning *Loss Ratio* is proposed in the quantitative analysis which expresses the relative size of the loss area

$$\textit{Loss Ratio} = \frac{\text{Area of the depth missing region}}{\text{Area of the entire target}}. \tag{18}$$

A larger *Loss Ratio* indicates the information loss is more significant.

From the quantitative outcomes in Fig. 11, a larger *Loss Ratio* results in worse MAE, compared target (a)- (b) to target (c)- (d), which means the relative area of the missing part limits the performance of the recovery algorithm to some extent, whereas the larger MAE is still acceptable

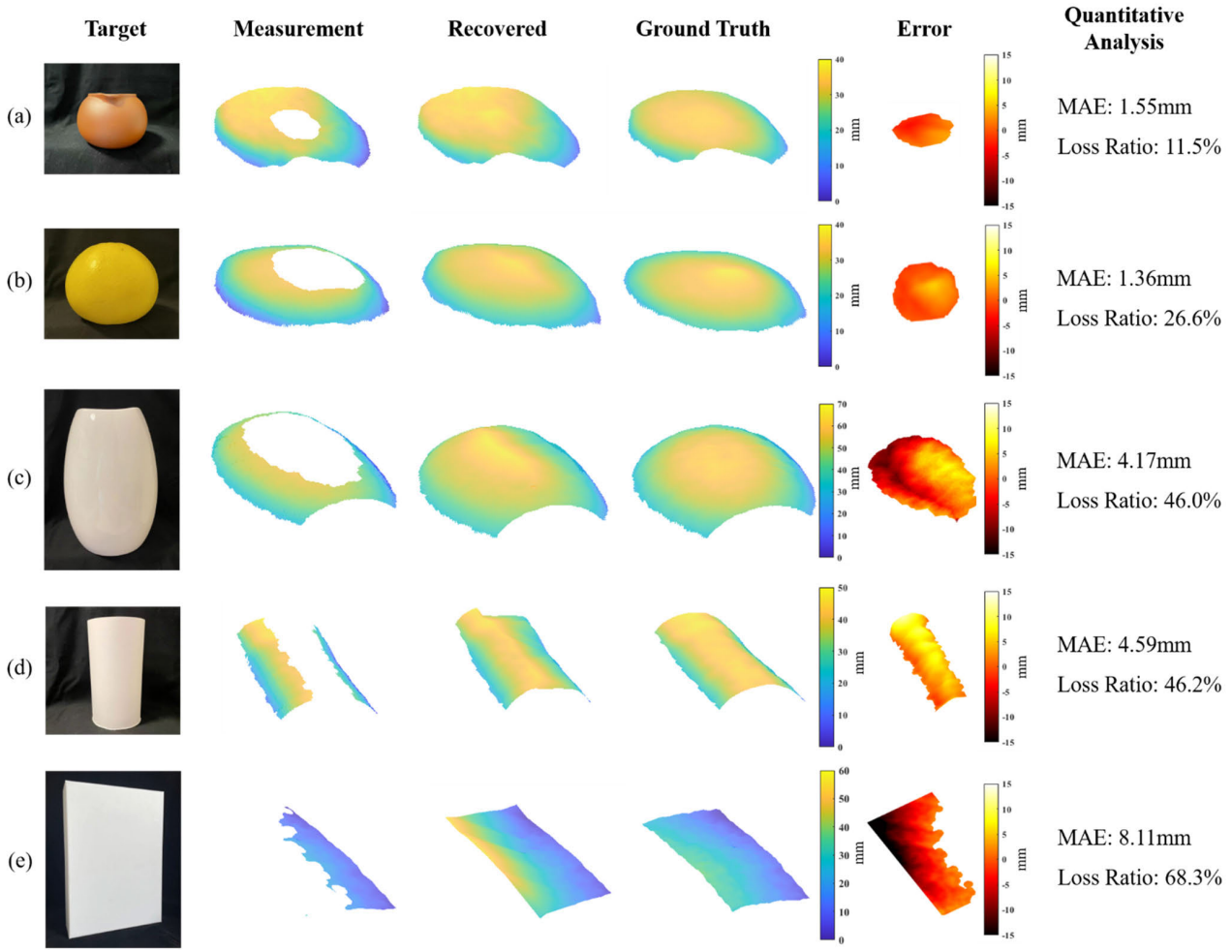

FIGURE 11. Experimental results after depth recovery for various targets qualitatively and quantitatively.

considering the size of the target and imaging distance in scenarios (a)- (d). However, scene (e) has an unacceptable poor performance, especially in the marginal region. The inaccuracy is partly because of the large *Loss Ratio*, but most importantly due to error accumulation in the marginal area. The accumulation of error is more significant as the recovered pixel is farther away from the depth known area under large *Loss Ratio* conditions.

Moreover, the recovery performance in diffuse targets ((a) & (d)) is comparatively inferior since the *DOP* value in diffuse dominant reflection is relatively smaller than specular dominant reflections according to Fig.5, namely the signal-to-noise ratio is poor in *DOP* map under diffuse conditions.

Furthermore, the result of the proposed algorithm is compared with additional proper depth recovery approaches in Fig. 12. Since most existed methods aim at recovery for structure-based holes instead of large-area depth missing, the existed techniques are unavailable to implement in the aforementioned experimental scenarios directly. In self-guided approach, missing depth is recovered according to the depth structure of the surrounding area. For RGB-guided method, depth recovery is guided by the calibrated flawless color image, in which equivalent RGB value indicates identical depth data. SfP-based approach is referred to [31]. Other existed algorithms which mainly deal with small-area structure-based depth loss fail to recover the large-area depth loss.

Fig.12 shows that the proposed polarization-guided approach possesses the optimal performance. Specifically, in self-guided attempt, the depth structure of the missing part is generally nonuniform with the depth pattern of the surrounding area, filling the holes with similar structure of the neighboring region is inappropriate especially for large-area holes, even though only one depth sensor is enough in this method which is more compact than RGB-D or Pol-D system. RGB-guided approach is more prevail benefited from the maturity of RGB-D cameras. In large-area depth filling cases, depth recovery is guided by R-G-B values via image processing methods since R-G-B value varies according to the target profile in visible image. However, RGB-guided approach lacks physical basics between depth and RGB data which generally leads to inaccuracy or artifacts. Mistakes due to the mixture of specular and diffuse components and azimuth angle ambiguity result in poor recovery in SfP-based

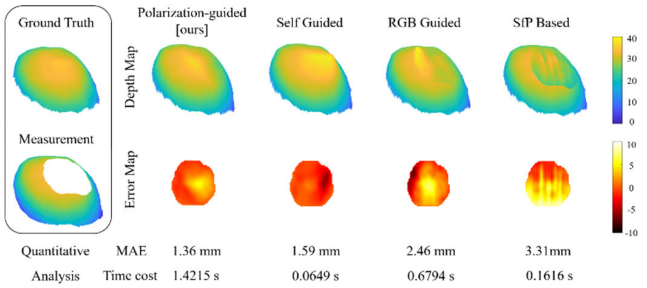

FIGURE 12. Qualitative and quantitative comparison results with additional depth recovery approaches.

outcomes. Compared with SfP-based technique, the proposed polarization-guided algorithm is more computational effective and avoids from the technical difficulties like specular-diffuse component separation, ambiguity treatment etc.

Additionally, the computation cost is also explored among the proposed algorithm and comparative approaches under identical processor, as shown in the quantitative analysis of Fig.12. The proposed method is more time-consuming because both LUT establishment and depth recovery procedures are implemented pixel-by-pixel instead of parallel. However, the time cost can be optimized through algorithm modification which will be discussed in detail in Section VI-C. Memory cost is also worth to be taken into consideration. Whereas, the proposed algorithm has almost equivalent memory cost with other comparative methods, which mainly depends on the size of the reconstructed target.

In conclusion, the proposed prototype for large-area depth recovery guided by polarization cues is applicable to targets in different kinds of materials without the requirement for reflection components and avoiding refractive index estimation. The method performance is related to the relative size of the loss area. Improvements can be studied concerning the effectiveness under large *Loss Ratio* conditions and computational time cost, which is furtherly discussed in Section VI-C.

VI. DISCUSSIONS

A. SELECTION OF N_1 AND N_2

The criterion of the selection concerning the filter size, N_1 and N_2, in Section IV-B and IV-C is explored with simulated data. Simulated depth map with holes and flawless *DOP* maps, both with added noise and known shape, are generated as inputs. Under identical simulated data but various filter sizes, output with lower MAE indicates a more reasonable filter size after depth inpainting with the proposed algorithm.

The simulation illustrates that the *Loss Ratio* of the detected scene in depth map and the resolution of the image sensor are two of the most significant factors which influence the optimal determination of N_1 and N_2. Results with a large range of simulated filter size N_1 under different resolutions and *Loss Ratio* are plotted in Fig. 13.

Fig. 13(a) shows that with a certain *Loss Ratio*, the impact in recovery accuracy related with N_1 decreases as the resolution increases, which means selection of N_1 is more sensitive with lower resolution, conversely the size of N_1 will not influences the recovered quality if the resolution is higher enough. Meanwhile, Fig.13(b) illustrates that N_1 is more irrelative towards the recovered precision if the *Loss Ratio* is limited (*Loss Ratio* less than 20%).

In summary, an empirical referenced table for the selection of N_1 is summarized in Fig. 14. As Fig. 13 indicates, filter size of N_1 in a certain range will not terrifically affect the quality of the recovered depth map, thus, a rough value of N_1 is necessary enough for the selection. The referenced table is given based on several common resolutions among off-the-shelf TOF sensors. N_1 selection under resolution or *Loss Ratio* out of the table can be referenced by nearby parameters or through interpolation. On the other hand, the selection of N_2 depends on the resolution to some extent, but has little influence on the recovery quality. Empirically, $N_2 = \frac{1}{2}N_1$ is reasonable.

B. STRENGTHS

The polarization-guided depth recovery method is inspired by the combination of RGB-D prototype and SfP techniques, but overcomes a series of challenges in SfP to a large extent. Compared to depth recovery guided by RGB pictures, polarization-guided algorithm is based on a fixed physical relation between depth and polarization cues, which is more convincing and more applicable in large-area depth missing conditions, realizing high dynamic range in depth sensing.

In the framework, specular and diffuse reflections can be treated as a mixture and don't need to be distinguished according to the different relations written in (10)-(11). The mixture of specular and diffuse components is the most common condition in practice which emphasized the advantage of generalizability possessed by the proposed algorithm.

Also, the proposed depth recovery framework has taken the common technical issues into account for the sake of better performance and robustness, for example, the noise resistance ability, avoidance of error accumulation in successive procedures and generalizability in applications. LUT establishment and G^{xy} calculation are implemented in a certain neighborhood to prevent inaccuracy due to random noise occurring in each pixel, which greatly suppresses the influence of noise generated in the image capture stage.

As mentioned in Section III, the proposed framework replaced the sophisticated steps in computation strictly based on the physical and mathematical basics with statistics and image processing attempts, which improve computational efficiency and prevent error accumulation in mathematical calculations.

C. LIMITATIONS AND FUTURE WORKS

Technical limitations still exist in this prototype. As mentioned in Section IV, the surveyed target is better to be homogenous in refractive index and the surface height has to be continuously changed, which means the framework is more useful in single target reconstruction. For more comprehensive 3D reconstruction applications like indoor

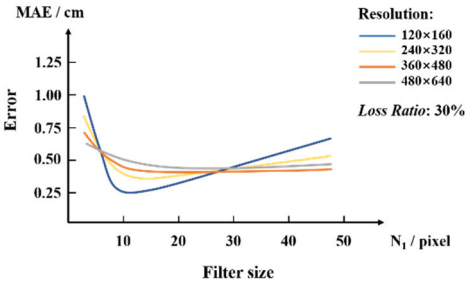

(a) N_1-MAE with various resolutions

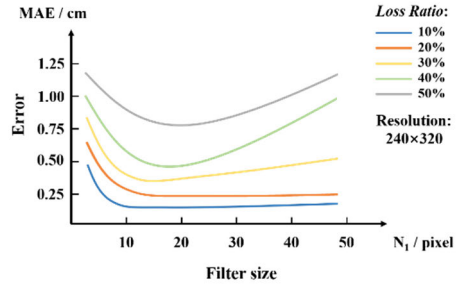

(b) N_1-MAE with various *Loss Ratio*

FIGURE 13. Relation between filter size (N_1) and recovered quality under different conditions.

Resolution \ LR	10%	20%	30%	40%	50%
120×160	10	10	10	15	15
240×320	10	10	15	15	20
360×480	15	15	15	20	25
480×640	20	20	20	25	25

* LR = *Loss Ratio*

FIGURE 14. Empirical referenced table for the N_1 selection.

reconstruction and robotic navigation, improvements can be investigated by combining the proposed method with existing RGB-D recovery approaches since RGB-D approaches are good at depth recovery in edge-area and the proposed one works well in large-area depth loss.

In Section V, the performance is getting worse as the *Loss Ratio* increases and the proposed algorithm is quite time-consuming. Both of the limitations can be optimized by dividing the whole scene into several patches and executing the proposed algorithm inside each patch in parallel, avoiding error accumulation. Furtherly, equipped with the optimized patch-based algorithm, complex targets with more details and textures can be recovered.

In addition, depth missing is a common problem in 3D reconstruction techniques. Besides depth loss in TOF imaging, the polarization-guided depth recovery method can be applied to depth missing in other 3D imaging approaches like stereo vision and structured light, for instance, depth missing occurs in the texture-less region for stereo vision and structured light suffers from data loss when affected by ambient light.

VII. CONCLUSION

A prototype of polarization-guided depth recovery method is proposed for large-area data loss in this paper, based on the physical model between degree-of-polarization and depth-gradient, realizing high dynamic range depth sensing and high-quality 3D reconstruction. A corresponding image processing algorithm and overall framework are illustrated in detail. The performance of the proposed method is verified qualitatively and quantitively via various targets and comparisons between multiple approaches. The limitations and future works are discussed as well. In conclusion, the proposed Pol-D method is effective in large-area depth missing benefited from the physical basics between polarization cues and depth map, with higher accuracy and free from sophisticated computations, which has great potentials in the technical progress of 3D reconstruction and depth measurement.

ACKNOWLEDGMENT

The authors would like to thank Yixin Zhang for providing the technical support.

REFERENCES

[1] L. Gomes, O. Bellon, and L. Silva, "3D reconstruction methods for digital preservation of cultural heritage: A survey," *Pattern Recognit. Lett.*, vol. 50, pp. 3–14, Dec. 2014.
[2] K. Chen, Y.-K. Lai, and S.-M. Hu, "3D indoor scene modeling from RGB-D data: A survey," *Comput. Vis. Media*, vol. 1, no. 4, pp. 267–278, 2015.
[3] X. Ma, Z. Wang, H. Li, P. Zhang, W. Ouyang, and X. Fan, "Accurate monocular 3D object detection via color-embedded 3D reconstruction for autonomous driving," in *Proc. IEEE/CVF Int. Conf. Comput. Vis. (ICCV)*, Seoul, South Korea, Oct. 2019, pp. 6851–6860.
[4] Z. Ma and S. Liu, "A review of 3D reconstruction techniques in civil engineering and their applications," *Adv. Eng. Informat.*, vol. 37, pp. 163–174, Aug. 2018.
[5] F. Remondino and D. Stoppa, *TOF Range-Imaging Cameras*. Trento, Italy: Springer, 2013, pp. 69–89.
[6] M. Dubreuil, P. Delrot, I. Leonard, A. Alfalou, C. Brosseau, and A. Dogariu, "Exploring underwater target detection by imaging polarimetry and correlation techniques," *Appl. Opt.*, vol. 52, no. 5, pp. 997–1005, Feb. 2013.
[7] J. Liang, L. Ren, H. Ju, W. Zhang, and E. Qu, "Polarimetric dehazing method for dense haze removal based on distribution analysis of angle of polarization," *Opt. Exp.*, vol. 23, no. 20, pp. 26146–26157, Oct. 2015.
[8] K. Berger, R. Voorhies, and L. H. Matthies, "Depth from stereo polarization in specular scenes for urban robotics," in *Proc. IEEE Int. Conf. Robot. Autom. (ICRA)*, May 2017, pp. 1966–1973.
[9] A. Sarafraz, S. Negahdaripour, and Y. Y. Schechner, "Enhancing images in scattering media utilizing stereovision and polarization," in *Proc. Workshop Appl. Comput. Vis. (WACV)*, Snowbird, UT, USA, Dec. 2009, pp. 1–8.
[10] X. Huang, J. Bai, K. Wang, Q. Liu, Y. Luo, K. Yang, and X. Zhang, "Target enhanced 3D reconstruction based on polarization-coded structured light," *Opt. Exp.*, vol. 25, no. 2, pp. 1173–1184, 2017.
[11] X. Huang, Y. Luo, J. Bai, R. Cheng, K. He, K. Wang, Q. Liu, Y. Luo, and J. Du, "Polarimetric target depth sensing in ambient illumination based on polarization-coded structured light," *Appl. Opt.*, vol. 56, no. 27, pp. 7741–7748, 2017.
[12] Y. Zhao, X. Wang, Y. Zhang, Y. Fang, and B. Su, "Polarization-based approach for multipath interference mitigation in time-of-flight imaging," *Appl. Opt.*, vol. 61, no. 24, pp. 7206–7217, Aug. 2022.
[13] Y. Zhang, X. Wang, Y. Zhao, and Y. Fang, "Time-of-flight imaging in fog using polarization phasor imaging," *Sensors*, vol. 22, no. 9, p. 3159, Apr. 2022.
[14] S. Rahmann and N. Canterakis, "Reconstruction of specular surfaces using polarization imaging," in *Proc. IEEE Comput. Soc. Conf. Comput. Vis. Pattern Recognit. CVPR*, Kauai, HI, USA, Aug. 2001, p. 1.

[15] A. Atapour-Abarghouei and T. P. Breckon, "A comparative review of plausible hole filling strategies in the context of scene depth image completion," *Comput. Graph.*, vol. 72, pp. 39–58, May 2018.
[16] M. A. Garduño-Ramón, I. R. Terol-Villalobos, R. A. Osornio-Rios, and L. A. Morales-Hernandez, "A new method for inpainting of depth maps from time-of-flight sensors based on a modified closing by reconstruction algorithm," *J. Vis. Commun. Image Represent.*, vol. 47, pp. 36–47, Aug. 2017.
[17] H. Xue, S. Zhang, and D. Cai, "Depth image inpainting: Improving low rank matrix completion with low gradient regularization," *IEEE Trans. Image Process.*, vol. 26, no. 9, pp. 4311–4320, Sep. 2017.
[18] J. Mao, J. Li, F. Li, and C. Wan, "Depth image inpainting via single depth features learning," in *Proc. 13th Int. Congr. Image Signal Process., Biomed. Eng. Informat. (CISP-BMEI)*, Chengdu, China, Oct. 2020, pp. 116–120.
[19] Y. S. Kim, "Closed-form solution of simultaneous denoising and hole filling of depth image," in *Proc. 25th IEEE Int. Conf. Image Process. (ICIP)*, Athens, Greece, Oct. 2018, pp. 968–972.
[20] D. Miao, J. Fu, Y. Lu, S. Li, and C. W. Chen, "Texture-assisted Kinect depth inpainting," in *Proc. IEEE Int. Symp. Circuits Syst.*, Seoul, South Korea, May 2012, pp. 604–607.
[21] J. Park, H. Kim, Y. Tai, M. S. Brown, and I. S. Kweon, "High-quality depth map upsampling and completion for RGB-D cameras," *IEEE Trans. Image Process.*, vol. 23, no. 12, pp. 5559–5572, Dec. 2014.
[22] W. Dong, G. Shi, X. Li, K. Peng, J. Wu, and Z. Guo, "Color-guided depth recovery via joint local structural and nonlocal low-rank regularization," *IEEE Trans. Multimedia*, vol. 19, no. 2, pp. 293–301, Feb. 2017.
[23] Z. Yan, L. Yu, and Z. Xiong, "Large-area depth recovery for RGB-D camera," in *Proc. IEEE Int. Conf. Image Process. (ICIP)*, Quebec City, QC, Canada, Sep. 2015, pp. 1409–1413.
[24] J. Liu, X. Gong, and J. Liu, "Guided inpainting and filtering for Kinect depth maps," in *Proc. 21st Int. Conf. Pattern Recognit. (ICPR)*, Tsukuba, Japan, Nov. 2012, pp. 2055–2058.
[25] H.-T. Zhang, J. Yu, and Z.-F. Wang, "Probability contour guided depth map inpainting and superresolution using non-local total generalized variation," *Multimedia Tools Appl.*, vol. 77, no. 7, pp. 9003–9020, Apr. 2018.
[26] F. Qi, J. Han, P. Wang, G. Shi, and F. Li, "Structure guided fusion for depth map inpainting," *Pattern Recognit. Lett.*, vol. 34, no. 1, pp. 70–76, Jan. 2013.
[27] J. Yang, X. Ye, K. Li, C. Hou, and Y. Wang, "Color-guided depth recovery from RGB-D data using an adaptive autoregressive model," *IEEE Trans. Image Process.*, vol. 23, no. 8, pp. 3443–3458, Aug. 2014.
[28] P. Lasang, W. Kumwilaisak, Y. Liu, and S. M. Shen, "Optimal depth recovery using image guided TGV with depth confidence for high-quality view synthesis," *J. Vis. Commun. Image Represent.*, vol. 39, pp. 24–39, Aug. 2016.
[29] C. Chen, J. Cai, J. Zheng, T. J. Cham, and G. Shi, "Kinect depth recovery using a color-guided, region-adaptive, and depth-selective framework," *ACM Trans. Intell. Syst. Technol.*, vol. 6, no. 2, pp. 1–19, Mar. 2015.
[30] Y. Zhang and T. Funkhouser, "Deep depth completion of a single RGB-D image," in *Proc. IEEE/CVF Conf. Comput. Vis. Pattern Recognit.*, Salt Lake City, UT, USA, Jun. 2018, pp. 175–185.
[31] T. Yoshida, V. Golyanik, O. Wasenmuller, and D. Stricker, "Improving time-of-flight sensor for specular surfaces with shape from polarization," in *Proc. 25th IEEE Int. Conf. Image Process. (ICIP)*, Athens, Greece, Oct. 2018, pp. 1558–1562.
[32] A. Kadambi, V. Taamazyan, B. Shi, and R. Raskar, "Polarized 3D: High-quality depth sensing with polarization cues," in *Proc. IEEE Int. Conf. Comput. Vis. (ICCV)*, Santiago, Chile, Dec. 2015, pp. 3370–3378.
[33] A. Kadambi, V. Taamazyan, B. Shi, and R. Raskar, "Depth sensing using geometrically constrained polarization normals," *Int. J. Comput. Vis.*, vol. 125, nos. 1–3, pp. 34–51, Dec. 2017.
[34] G. A. Atkinson and E. R. Hancock, "Recovery of surface orientation from diffuse polarization," *IEEE Trans. Image Process.*, vol. 15, no. 6, pp. 1653–1664, Jun. 2006.
[35] D. Miyazaki, T. Shigetomi, M. Baba, R. Furukawa, S. Hiura, and N. Asada, "Polarization-based surface normal estimation of black specular objects from multiple viewpoints," in *Proc. 2nd Int. Conf. 3D Imag., Model., Process., Visualizat. Transmiss.*, Zurich, Switzerland, Oct. 2012, pp. 104–111.
[36] D. Miyazaki, M. Saito, Y. Sato, and K. Ikeuchi, "Determining surface orientations of transparent objects based on polarization degrees in visible and infrared wavelengths," *J. Opt. Soc. Am. A*, vol. 19, no. 4, pp. 687–694, Apr. 2002.
[37] G. A. Atkinson and E. R. Hancock, "Surface reconstruction using polarization and photometric stereo," in *Proc. 12th Int. Conf. Comput. Anal. Images Patterns*, Aug. 2007, pp. 466–473.
[38] Z. Cui, J. Gu, B. Shi, P. Tan, and J. Kautz, "Polarimetric multi-view stereo," in *Proc. IEEE Conf. Comput. Vis. Pattern Recognit. (CVPR)*, Honolulu, HI, USA, Jul. 2017, pp. 1558–1567.
[39] T. Thanh Ngo, H. Nagahara, and R.-I. Taniguchi, "Shape and light directions from shading and polarization," in *Proc. IEEE Conf. Comput. Vis. Pattern Recognit. (CVPR)*, Boston, MA, USA, Jun. 2015, pp. 2310–2318.
[40] V. Taamazyan, A. Kadambi, and R. Raskar, "Shape from mixed polarization," 2016, *arXiv:1605.02066*.

YUWEI ZHAO received the B.S. degree from the Beijing Institute of Technology, in 2020, where she is currently pursuing the M.S. degree with the Key Laboratory of Optoelectronic Imaging Technology and Systems. Her research interests include time-of-flight imaging and polarization imaging.

XIA WANG received the Ph.D. degree in automation from the China University of Mining and Technology, in 1999. She is currently an Associate Professor with the Beijing Institute of Technology, where she is also the Vice Dean of the Institute of Photoelectric Imaging and Information Engineering. Her current research interests include optoelectronic detection, spectrum analysis, and imaging technology.

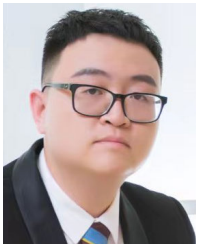

YUJIE FANG received the M.S. degree from Xi'an Technological University, in 2012. He is currently pursuing the Ph.D. degree with the Key Laboratory of Optoelectronic Imaging Technology and Systems, Beijing Institute of Technology, Zhuhai. He is currently an Associate Professor with the Beijing Institute of Technology. His current research interests include time-of-flight imaging, none-line-of-sight imaging, and optoelectronic detection.

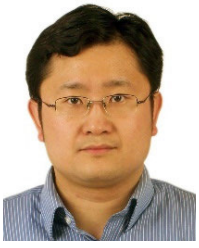

CHAO XU received the Ph.D. degree in optical engineering from the Beijing Institute of Technology, in 2006. He is currently a Lecturer and a Supervisor with the Key Laboratory of Optoelectronic Imaging Technology and Systems, Beijing Institute of Technology. His current research interests include optoelectronic imaging technology, photoelectric systems, and high-speed and real-time imaging technology.